

Dzyaloshinskii–Moriya-driven instabilities in square-kagome quantum antiferromagnets

Leonid S. Taran,^{1,*} Arnaud Ralko,^{2,3,*} Fedor V. Temnikov,^{1,*}
Vladimir V. Mazurenko,⁴ Sergey V. Streltsov,^{1,3,4} and Yasir Iqbal^{3,†}

¹*M. N. Mikheev Institute of Metal Physics, Ural Branch of Russian Academy of Sciences, 620137 Ekaterinburg, Russia*

²*Institut Néel, Université Grenoble Alpes, CNRS, Grenoble INP, 38000 Grenoble, France*

³*Department of Physics, Indian Institute of Technology Madras, Chennai 600036, India*

⁴*Department of Theoretical Physics and Applied Mathematics,
Ural Federal University, Mira St. 19, 620002 Ekaterinburg, Russia*

(Dated: March 12, 2026)

Decorated square-kagome quantum antiferromagnets provide a natural setting in which strong frustration, lattice decoration, and spin–orbit-induced anisotropy compete on comparable energy scales. Here we show that in $\text{Na}_6\text{Cu}_7\text{BiO}_4(\text{PO}_4)_4\text{Cl}_3$ the coupling (J_{10}) which links the decorating Cu(3) sites to the square-kagome backbone, stabilizes the gapped quantum-paramagnetic regime, while symmetry-allowed Dzyaloshinskii–Moriya (DM) interactions systematically suppress the minimum spinon gap Δ_{spinon} and drive the system toward magnetic condensation. To establish this, we combine *ab initio* calculation of the DM vectors with a generalized Schwinger-boson self-consistent mean-field theory that treats singlet and triplet hopping/pairing channels on equal footing. As a benchmark, the isotropic square-kagome Heisenberg model exhibits four competing low-energy saddle points distinguished by their Wilson-loop fluxes and by characteristic static and dynamical structure-factor fingerprints. A minimal DM perturbation does not qualitatively reshape this competing landscape, but already enhances the tendency towards order. For the realistic decorated Hamiltonian, finite-size scaling of Δ_{spinon} together with momentum-resolved structure factors identifies J_{10} (exchange with decorating Cu) as the control parameter of the gapped regime and shows that the full symmetry-allowed DM pattern shifts the system further toward condensation. Our results place $\text{Na}_6\text{Cu}_7\text{BiO}_4(\text{PO}_4)_4\text{Cl}_3$ in close proximity to a magnetic instability and provide experimentally testable predictions for anisotropy-enhanced soft modes in decorated square-kagome materials.

I. INTRODUCTION

Frustrated quantum magnets built from corner-sharing motifs continue to provide a fertile setting for unconventional collective behavior, including dense low-energy spectra, strong renormalization of thermodynamic scales, and quantum-disordered ground states. Within this broader landscape, the square-kagome (shuriken) lattice occupies a distinctive position [1]. Like kagome, it combines strong geometric frustration with corner-sharing triangles, but it also hosts square plaquettes, flat-band physics, and a different hierarchy of competing ordered and disordered states [2–6]. As a result, the spin- $\frac{1}{2}$ square-kagome Heisenberg antiferromagnet has emerged as a nontrivial frustrated platform in its own right, with high-field anomalies [7–9], low-temperature thermodynamic signatures [10, 11], and competing valence-bond and ordered tendencies already established theoretically [3, 12–15].

This theoretical interest has been amplified by the recent emergence of square-kagome and decorated square-kagome materials. Hydrothermal synthesis and structural characterization of $\text{Na}_6\text{Cu}_7\text{BiO}_4(\text{PO}_4)_4[\text{Cl}(\text{OH})]_3$ established a prominent Cu^{2+} -based realization in which a square-kagome layer is decorated by an additional magnetic Cu site [16–18]. Low-temperature thermodynamic measurements on $\text{Na}_6\text{Cu}_7\text{BiO}_4(\text{PO}_4)_4[\text{Cl}(\text{OH})]_3$ and related compounds revealed the absence of conventional long-range order down to

very low temperatures together with a pronounced low-energy sector [19, 20]. At the same time, the broader nabokoite family and related tellurate–sulfate compounds [21–26] have expanded the experimental landscape of decorated and distorted square-kagome magnets, making it increasingly necessary to go beyond idealized isotropic nearest-neighbor models [27]. These developments elevate square-kagome magnetism from a model curiosity to a growing materials platform.

A key lesson from this materials progress is that the relevant exchange networks are not only frustrated but also structurally low-symmetry. The present work is motivated by the fact that in low-symmetry Cu–O–Cu environments relevant to decorated square-kagome materials, Dzyaloshinskii–Moriya (DM) interactions are not a secondary correction but a symmetry-allowed perturbation of experimentally relevant magnitude. The antisymmetric exchange introduced by Dzyaloshinskii and Moriya [28, 29] is well known to qualitatively reshape frustrated spin- $\frac{1}{2}$ magnets by lowering spin-rotation symmetry, admixing chiral correlations, and stabilizing magnetic order out of nearby quantum-disordered regimes. In kagome antiferromagnets, for example, DM interactions shift phase boundaries, modify excitation spectra, and enhance condensation tendencies within Schwinger-boson descriptions [30, 31]. In the square-kagome setting, where competing states are already close in energy, the effect of symmetry-allowed DM interactions is therefore a central and unavoidable question.

This issue is especially acute for decorated square-kagome compounds. In our recent work on $\text{Na}_6\text{Cu}_7\text{BiO}_4(\text{PO}_4)_4\text{Cl}_3$, we established a realistic antiferromagnetic Hamiltonian and showed that the material remains quantum paramagnetic despite the presence of the decorating Cu^{2+} site [32]. An im-

* These authors contributed equally.

† yiqbal@physics.iitm.ac.in

portant outcome of that work was that the decorating site is not inert: the coupling J_{10} , which connects the decorating apical Cu(3) sites to the square-kagome backbone, plays an active role in stabilizing the disordered regime. This immediately raises the next microscopic question: how robust is that quantum-paramagnetic regime once symmetry-allowed anisotropic exchange is included? More specifically, does DM merely perturb the disordered state, or does it systematically drive the system toward magnetic condensation?

In this paper we show that the latter question is governed by a simple and physically transparent mechanism. In decorated square-kagome antiferromagnets, J_{10} stabilizes the quantum-paramagnetic regime, while symmetry-allowed DM interactions systematically destabilize it and drive the system toward magnetic ordering. To establish this, we combine two complementary ingredients. First, we extract the full symmetry-allowed DM vectors for $\text{Na}_6\text{Cu}_7\text{BiO}_4(\text{PO}_4)_4\text{Cl}_3$ from *ab initio* calculations incorporating spin-orbit-coupling. Second, we analyze both the ideal and material-specific Hamiltonians within a generalized Schwinger-boson self-consistent mean-field theory that treats singlet and triplet hopping/pairing channels on equal footing [33–35]. This framework allows us to track how anisotropy reshapes the spinon spectrum, shifts the proximity to boson condensation, and modifies equal-time and dynamical correlation signatures.

Our analysis proceeds in two steps. We first benchmark the generalized formalism on the isotropic square-kagome model, where we identify the competing low-energy saddle points and test the effect of a minimal DM perturbation. We then turn to the realistic compound Hamiltonian of $\text{Na}_6\text{Cu}_7\text{BiO}_4(\text{PO}_4)_4\text{Cl}_3$, where the central result emerges: the coupling J_{10} acts as the control parameter stabilizing the gapped regime, while the symmetry-allowed DM pattern suppresses the minimum spinon gap and enhances the tendency toward ordering. This places the material in close proximity to a magnetic instability and yields experimentally testable predictions for anisotropy-enhanced soft modes and momentum-resolved spectral weight redistribution.

The remainder of the paper is organized as follows. In Sec. II we extract the isotropic exchanges and symmetry-allowed DM vectors for $\text{Na}_6\text{Cu}_7\text{BiO}_4(\text{PO}_4)_4\text{Cl}_3$ from *ab initio* calculations and summarize the resulting microscopic Hamiltonian. In Sec. III we introduce the generalized Schwinger-boson formalism, define the Wilson-loop diagnostics, and describe the numerical protocol. In Sec. IV we present the results for the isotropic square-kagome benchmark, the minimal DM perturbation test, and the realistic compound Hamiltonian, including the evolution of the minimum spinon gap and the corresponding equal-time and dynamical structure factors. Finally, in Sec. V we summarize the physical implications for decorated square-kagome quantum antiferromagnets and for ongoing experiments on this growing materials family.

II. DM VECTORS EXTRACTION FROM DFT CALCULATIONS

The crystallographic data were taken from Ref. [16], and the crystal structure is shown in Fig. 1. The conventional unit cell contains two formula units of $\text{Na}_6\text{Cu}_7\text{BiO}_4(\text{PO}_4)_4\text{Cl}_3$, crystallizes in the tetragonal $P4/nmm$ space group. Each Cu ion is coordinated by four oxygen ligands forming square CuO_4 plaquettes. Given this local coordination environment and the fact that Cu^{2+} is a d^9 ion with spin $S = 1/2$, one expects the $x^2 - y^2$ orbital to remain half-filled and thus to dominate the low-energy electronic structure.

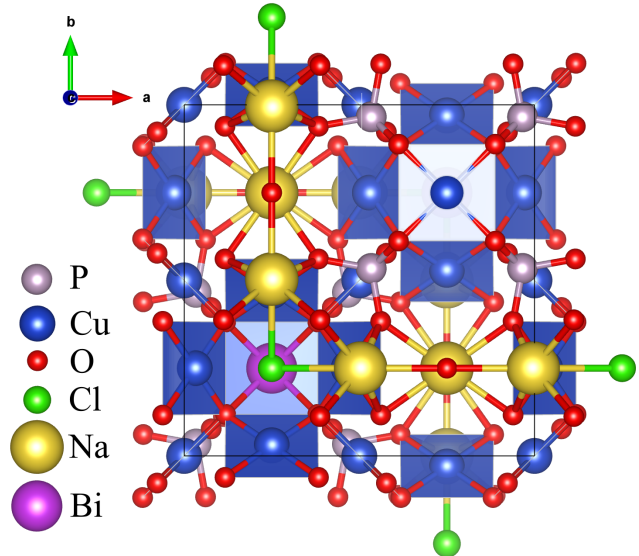


FIG. 1. Crystal structure of $\text{Na}_6\text{Cu}_7\text{BiO}_4(\text{PO}_4)_4\text{Cl}_3$. The Cu^{2+} ions occupy three crystallographically inequivalent positions, Cu(1), Cu(2), and Cu(3). Cu(1) and Cu(2) form the square-kagome backbone, while Cu(3) decorates it in a checkerboard manner above and below the square-kagome plane.

The band structure shown in Fig. 2 reveals a group of 14 bands near the Fermi level originating from the empty $\text{Cu } d_{x^2-y^2}$ states. These are separated from the remaining valence d states by an energy gap of 400 meV. Further details of the electronic structure are provided in the form of the density of states in Fig. 10 of Appendix A.

Within the unit cell, the Cu^{2+} ions occupy three crystallographically inequivalent positions, Cu(1), Cu(2), and Cu(3), indicated by different colors in Fig. 3. Cu(1) and Cu(2) form a square kagome lattice, while Cu(3) decorates it at the top and bottom in a checkerboard manner. The latter are not directly connected to other Cu atoms through shared oxygen ligands, making them isolated from the kagome lattice. These atoms form square plaquettes with a uniform Cu–O bond length of 1.959 Å.

The Cu(1) plaquettes exhibit elongation and adopt a rhombic shape. Here, the longer Cu–O bonds (1.952 Å) connect Cu(1) with Cu(2) atoms, while the shorter bonds (1.938 Å) link to the $[\text{PO}_4]$ tetrahedra.

The Cu(2) atoms not only interconnect with each other and

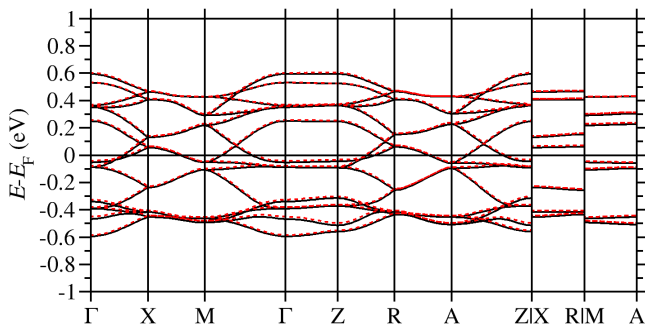


FIG. 2. Band structure of $\text{Na}_6\text{Cu}_7\text{BiO}_4(\text{PO}_4)_4\text{Cl}_3$ from nonmagnetic GGA calculations. Dashed red lines show the DFT bands, while solid black lines show the Wannier-interpolated bands obtained from the Cu $d_{x^2-y^2}$ orbitals used to estimate the exchange parameters via hopping integrals. The isolated 14-band manifold near the Fermi level supports the one-band low-energy description.

Cu(1), but are also attracted to bismuth atoms located above or below the center of the copper squares. This leads to a tilting of the CuO_4 plaquettes and results in a trapezoidal distortion with two distinct Cu–O bond lengths: a shorter pair (1.929 Å) and a longer pair (1.964 Å).

To estimate the parameters of exchange interaction, maximally localized Wannier functions corresponding to the Cu $x^2 - y^2$ orbitals were constructed. The distinct geometries of the plaquettes influence the hybridization and the band structure, and therefore also affect the spatial localization of the Wannier functions. As a result, the smallest WF spread, approximately ~ 2.9 Å, is observed for the isolated plaquettes formed by the decorating Cu(3) atoms, while the largest one, ~ 3.9 Å, appears for the trapezoidal plaquettes of the Cu(2) sites.

The isotropic exchange interactions were estimated using Anderson’s superexchange theory [36–38]:

$$J_{ij} = \frac{4t_{ij}^2}{U}, \quad (1)$$

where t_{ij} are the hopping integrals and U is the effective on-site Coulomb interaction for the one-band model. In Table I we present exchange couplings with $|J| > 4$ K (the full list of exchanges is presented in Table III of Appendix B).

For a reliable set of exchange parameters, good agreement between the theoretical and experimental Curie–Weiss temperatures is essential. Using the formula

$$\Theta = -\frac{S(S+1)}{3} \sum_{i \neq j} J_{ij}, \quad (2)$$

where the sum runs over all pairs of copper atoms within the unit cell using the exchange couplings from Table I, one finds $\Theta = -216$ K, -205 K, and -180 K for $U = 6.66$, 7, and 8 eV, respectively. These values can be compared with the experimentally measured Curie–Weiss temperature $\Theta_{\text{exp}} = -212$ K. The closest agreement is achieved for $U = 6.66$ eV, as in Ref. [32], where J_{ij} were calculated by the accurate total energy methods, containing contribution from

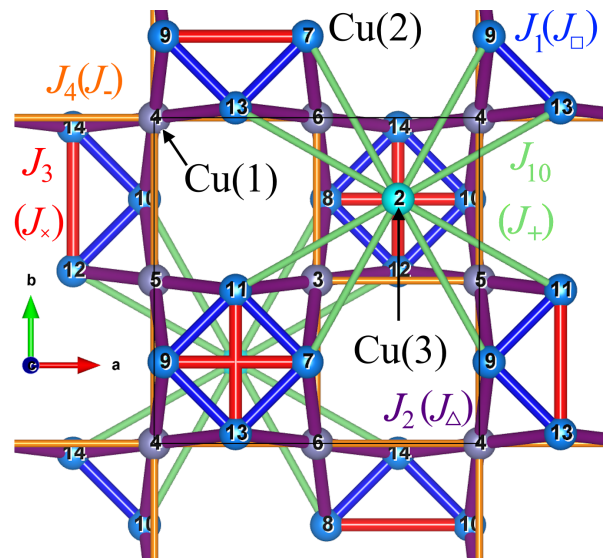


FIG. 3. Relevant exchange paths in $\text{Na}_6\text{Cu}_7\text{BiO}_4(\text{PO}_4)_4\text{Cl}_3$ with Cu sites labeled for clarity. Cu(1) and Cu(2) form the square-kagome backbone, while Cu(3) denotes the decorating sites. Colored bonds distinguish the different isotropic exchange couplings entering the microscopic spin Hamiltonian.

all possible exchange channels. This value of $U = 6.66$ eV is therefore adopted for all subsequent exchange-parameter calculations in $\text{Na}_6\text{Cu}_7\text{BiO}_4(\text{PO}_4)_4\text{Cl}_3$.

The extracted exchange hierarchy can be discussed in the light of the square-kagome phase diagram. According to Ref. [3, 13], which considers only nearest-neighbor (J_1) and next-nearest-neighbor (J_2) interactions, a non-magnetic singlet ground state with a finite spin gap separating singlet and triplet excitations is expected when $0.77 < J_2/J_1 < 1.65$. For $J_2/J_1 \gtrsim 1.65$, the system adopts a ferrimagnetic ground state. A similar ratio was reported in Ref. [32], with $J_2/J_1 \sim 1.7$. However, the presence of a substantial diagonal coupling J_3 ($J_3/J_1 \sim 1.45$) increases frustration and stabilizes a non-magnetic valence-bond crystal (VBC) ground state with broken translational symmetry.

In the present calculations, the ratio $J_2/J_1 \simeq 1.29$ clearly falls within the regime favoring a singlet ground state. This

J_N ($J_{\text{not.}}$)	d (Å)	$U=6.66$ eV	$U=7$ eV	$U=8$ eV	Ref.[32]
J_1 (J_\square)	3.114	157.7	150.0	131.3	109.2
J_2 (J_Δ)	3.278	202.8	193.0	168.8	186.3
J_3 (J_\times)	4.404	87.3	83.0	72.7	155.3
J_4 (J_-)	5.009	29.4	27.9	24.4	47.0
J_5	5.009	9.0	8.6	7.5	5.3
J_{10} (J_+)	6.018	47.8	45.5	39.8	64.6
J_{14}	7.084	5.0	4.8	4.2	1.9

TABLE I. Isotropic exchange interactions J_N and their notation $J_{\text{not.}}$ (in K) for $\text{Na}_6\text{Cu}_7\text{BiO}_4(\text{PO}_4)_4\text{Cl}_3$, estimated from Eq. (1) in the present work and compared with the DFT energy-mapping results of Niggemann *et al.* [32]. The exchange-path notation is defined in Fig. 3. Only couplings with $|J| > 4$ K are listed here; the full set is given in Table III.

conclusion remains valid even if one considers a smaller contribution coming from J_3 ($J_3/J_1 = 0.55$). Furthermore, the decorating Cu(3) sites exhibit a significant exchange coupling to the main kagome network via $J_{10} = 47.8$ K.

We next turn to the antisymmetric anisotropic exchange. The DM vector \mathbf{D}_{ij} is calculated using Moriya's superexchange theory [29, 37]:

$$\mathbf{D}_{ij} = \frac{i}{U} [\text{Tr}(\hat{t}_{ij})\text{Tr}(\hat{t}_{ji}\boldsymbol{\sigma}) - \text{Tr}(\hat{t}_{ji})\text{Tr}(\hat{t}_{ij}\boldsymbol{\sigma})], \quad (3)$$

where \hat{t}_{ij} is the hopping matrix including the spin-orbit coupling, and $\boldsymbol{\sigma}$ are the Pauli matrices. This approach has been successfully applied to other compounds in Refs. [39, 40].

To evaluate the Dzyaloshinskii–Moriya interaction (DMI) parameters, the corresponding Hamiltonian from calculations including spin-orbit coupling was derived. The largest final WF spread, ~ 3.8 Å, occurs for the rhombic plaquettes of the Cu(1) sites. The computed leading DMI parameters, represented by one bond from each symmetry-equivalent set, are presented in Table II, while the full list of estimated values is summarized in Appendix B, Table IV and V.

The DM vectors are defined in a global coordinate system aligned with the crystallographic axes of the unit cell. Due to the antisymmetric nature of the exchange, they satisfy the relation $\mathbf{D}_{ij} = -\mathbf{D}_{ji}$. All DM vectors of a given type are related by the symmetry operations of the space group $P4/nmm$. For instance, the transformation from the nearest-neighbor Cu7–Cu11 bond to the Cu13–Cu7 bond corresponds to a 90° rotation around the z axis. This operation leaves the z component of both the position vector and the Dzyaloshinskii–Moriya vector unchanged. Since the DM vector is axial, it remains invariant under inversion; therefore, the following relations must hold: $\mathbf{D}_{7-11} = \mathbf{D}_{8-12}$, $\mathbf{D}_{13-7} = \mathbf{D}_{14-8}$, $\mathbf{D}_{9-13} = \mathbf{D}_{10-14}$, and $\mathbf{D}_{11-9} = \mathbf{D}_{12-10}$. As demonstrated in Table IV in Appendix B, our calculations reproduce these relations with high accuracy.

The largest Dzyaloshinskii–Moriya interaction (DMI) parameters are found for the nearest-neighbor Cu(1)–Cu(1), Cu(1)–Cu(2), and next-nearest-neighbor Cu(1)–Cu(1) and Cu(2)–Cu(2) pairs, with magnitudes of approximately 14 K, 28 K, 9 K, and 11 K, respectively. All other DMI parameters, however, do not exceed 4 K.

The site-resolved sums of the DM vectors, $\mathbf{D}_i^{\text{eff}} = \sum_j \mathbf{D}_{ij}$, for all copper atoms are illustrated in Fig. 11 of Appendix B. It is worth noting that the direction of the total DM vector for the Cu(2) sites lies along one of the axes within the ab -plane and transforms via a 90° rotation around the z -axis (see Fig. 12 of Appendix B). Since the symmetry of the spin canting is defined by the symmetry of the magnetic torque, the rotation of the spins for the Cu(2) sublattice occurs within the plane perpendicular to the DM vector, i.e., in the ac - or bc -plane depending on the specific Cu(2) site orientation. In contrast, for the Cu(1) atoms, the total DM interaction is directed perpendicular to the Cu(1)O₄ plaquette planes. This geometry forces the spin rotation to occur strictly within the plane of the plaquettes. Finally, for the isolated decorating Cu(3) sites, the calculated total DM vector vanishes, indicating that the Dzyaloshinskii–Moriya interaction is negligible compared to

Bond m-n (not.)	\mathbf{R}_{mn}	\mathbf{D}_{mn}	$ \mathbf{D} $
7–11(\square)	(−2.2; 2.2; 0.0)	(5.8; 5.8; −11.2)	13.9
3–11(\triangle)	(−2.5; −0.3; 2.1)	(7.3; −19.1; −18.8)	27.7
11–13(\times)	(0.0; −4.4; 0.0)	(8.9; 0.0; 0.0)	8.9
3–5(−)	(−5.0; 0.0; 0.0)	(0.0; −10.8; 1.9)	11.0
2–11(+)	(−5.0; −2.8; −1.8)	(−1.7; −0.9; −2.8)	3.3

TABLE II. Representative Dzyaloshinskii–Moriya vectors \mathbf{D}_{mn} and their magnitudes (in K) for Na₆Cu₇BiO₄(PO₄)₄Cl₃ at $U = 6.66$ eV. One bond is shown for each symmetry-equivalent class, with the corresponding notation indicated in parentheses; all other equivalent DM vectors are generated by the crystallographic symmetry operations of space group $P4/nmm$. The bond labels refer to Fig. 3. The complete set of DM vectors is given in Tables IV and V.

the isotropic exchange J .

III. SCHWINGER-BOSON MEAN-FIELD THEORY AND NUMERICAL PROTOCOL

Schwinger-boson mean-field theory (SBMFT) provides a unified framework to describe quantum-disordered regimes and magnetically ordered phases in frustrated quantum magnets. In particular, it gives direct access to the excitation spectrum of the quadratic bosonic Hamiltonian and therefore enables the computation of experimentally relevant observables such as equal-time and dynamical spin structure factors. The formalism also naturally accommodates explicit SU(2) symmetry breaking, as induced by Dzyaloshinskii–Moriya (DM) interactions, through the inclusion of triplet hopping and pairing channels. Further methodological details can be found in Refs. [5, 41–44] and references therein.

A. Formalism for Heisenberg + DM interactions

In SBMFT the spin operator at site i is represented as

$$\hat{\mathbf{S}}_i = \frac{1}{2} \hat{b}_i^\dagger \vec{\sigma} \hat{b}_i, \quad (4)$$

where $\hat{b}_i^\dagger = (\hat{b}_{i\uparrow}^\dagger, \hat{b}_{i\downarrow}^\dagger)$ and $\vec{\sigma} = (\sigma^1, \sigma^2, \sigma^3)$ are the Pauli matrices. Physical spin- S states are recovered by imposing the local constraint

$$\hat{n}_i = \hat{b}_i^\dagger \hat{b}_i = 2S \equiv \kappa, \quad (5)$$

enforced on average via Lagrange multipliers λ_i .

We consider a Heisenberg–Dzyaloshinskii–Moriya Hamiltonian

$$\mathcal{H}_{\text{HDM}} = \sum_{i,j} J_{ij} \hat{\mathbf{S}}_i \cdot \hat{\mathbf{S}}_j + \sum_{i,j} \mathbf{D}_{ij} \cdot (\hat{\mathbf{S}}_i \times \hat{\mathbf{S}}_j). \quad (6)$$

To treat SU(2)-symmetric and SU(2)-breaking terms on equal footing, we introduce singlet and triplet hopping/pairing op-

erators

$$\hat{h}_{ij}^\alpha = \frac{1}{2} \hat{b}_i^\dagger \sigma^\alpha \hat{b}_j, \quad (7)$$

$$\hat{p}_{ij}^\alpha = \frac{i}{2} \hat{b}_i (\sigma^\alpha \sigma^2) \hat{b}_j, \quad (8)$$

with $\alpha = 0$ the singlet channel ($\sigma^0 = \mathbb{I}$) and $\alpha = 1, 2, 3$ the triplet channels. Using vector notations $\hat{\mathbf{h}}_{ij} = (\hat{h}_{ij}^0, \hat{h}_{ij}^1, \hat{h}_{ij}^2, \hat{h}_{ij}^3)^T$ and $\hat{\mathbf{p}}_{ij} = (\hat{p}_{ij}^0, \hat{p}_{ij}^1, \hat{p}_{ij}^2, \hat{p}_{ij}^3)^T$, the exchange terms can be rewritten as

$$\hat{\mathbf{S}}_i \cdot \hat{\mathbf{S}}_j = \hat{\mathbf{h}}_{ij}^\dagger m_0 \hat{\mathbf{h}}_{ij} : -\hat{\mathbf{p}}_{ij}^\dagger m_0 \hat{\mathbf{p}}_{ij}, \quad (9)$$

$$\mathbf{D}_{ij} \cdot (\hat{\mathbf{S}}_i \times \hat{\mathbf{S}}_j) = \hat{\mathbf{h}}_{ij}^\dagger m_{ij}^{\text{DM}} \hat{\mathbf{h}}_{ij} : -\hat{\mathbf{p}}_{ij}^\dagger m_{ij}^{\text{DM}} \hat{\mathbf{p}}_{ij}. \quad (10)$$

Here $m_0 = \text{diag}(1, -\frac{1}{3}, -\frac{1}{3}, -\frac{1}{3})$, while m_{ij}^{DM} is an antisymmetric 4×4 matrix encoding the orientation and magnitude of \mathbf{D}_{ij} (as defined in Sec. II). The DM interaction thus couples naturally to triplet channels and explicitly breaks SU(2) symmetry.

The resulting Schwinger-boson Hamiltonian reads

$$\mathcal{H}_{\text{SB}} = \sum_{i,j} \left[: \hat{\mathbf{h}}_{ij}^\dagger H_{ij} \hat{\mathbf{h}}_{ij} : + \hat{\mathbf{p}}_{ij}^\dagger P_{ij} \hat{\mathbf{p}}_{ij} \right] + \sum_i \lambda_i (\hat{n}_i - \kappa), \quad (11)$$

with $H_{ij} = J_{ij} m_0 + m_{ij}^{\text{DM}}$ and $P_{ij} = -H_{ij}$. A mean-field decoupling is performed by introducing $\mathbf{h}_{ij} = \langle \hat{\mathbf{h}}_{ij} \rangle$ and $\mathbf{p}_{ij} = \langle \hat{\mathbf{p}}_{ij} \rangle$, evaluated in the bosonic vacuum $|\phi_0\rangle$. The quadratic Hamiltonian is diagonalized via a bosonic Bogoliubov transformation, yielding the spinon bands and enabling the computation of correlation functions.

B. Numerical protocol, stability checks, and observables

Self-consistency was initialized from multiple starting configurations, including (i) fully random mean-field amplitudes and (ii) symmetry-distinct flux seeds used in the square-kagome SBMFT literature. The converged solutions reported in this work correspond to stable fixed points of the self-consistency cycle: small perturbations of the converged amplitudes systematically flow back to the same solution upon iteration. Calculations were performed on clusters of size $N = n_u \times l^2$ sites, with n_u the number of sites in the unit cell, up to $N = 1944$ spins for the isotropic square-kagome model ($n_u = 6, l = 18$) and up to $N = 4032$ sites for the realistic compound Hamiltonian ($n_u = 28, l = 12$) in the regime of small J_{10} . The momentum resolution and spectral broadening used for the dynamical structure factors were checked such that the qualitative features discussed below are insensitive to these numerical parameters. The Brillouin zones corresponding to the two unit cells, together with the high-symmetry points and the momentum paths used to compute the dynamical structure factors, are shown in Fig. 4.

We work on finite clusters, which introduce a small finite-size spinon gap even when the thermodynamic system is expected to condense. This controlled finite-size gap prevents

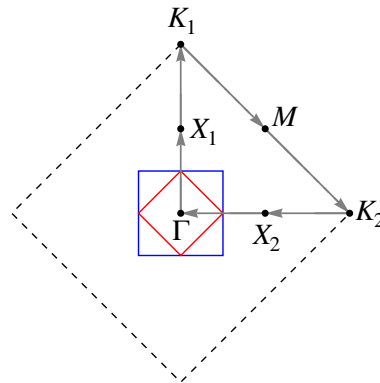


FIG. 4. First Brillouin zones corresponding to the different unit cells considered in this work: the square-kagome lattice with $n_u = 6$ sites per unit cell (blue), the enlarged unit cell with $n_u = 14$ sites (red), and the underlying square lattice (black dashed). High-symmetry points are indicated, and the gray arrows denote the momentum path used to compute the dynamical spin structure factors.

immediate Bose condensation up to a certain critical S and allows us to monitor ordering tendencies continuously through clear precursors of mode softening, either via the suppression of the minimum spinon gap or through the redistribution of spectral weight in the dynamical structure factor.

To characterize gauge-inequivalent mean-field states, we use Wilson-loop (WL) fluxes constructed from the complex pairing amplitudes [45, 46]. On the square-kagome lattice a natural choice is to consider elementary six-site loops [41]. For a generic loop $\mathcal{C} = (i \rightarrow j \rightarrow k \rightarrow l \rightarrow m \rightarrow n \rightarrow i)$, the associated WL is defined as

$$W_{\mathcal{C}} = \arg [p_{ij}^0 (-p_{jk}^{0*}) p_{kl}^0 (-p_{lm}^{0*}) p_{mn}^0 (-p_{ni}^{0*})], \quad (12)$$

which is invariant under local gauge transformations and therefore provides a gauge-independent flux threading the loop. Each SBMFT saddle point can then be labeled by the set of inequivalent WL fluxes within a unit cell, which we denote as $\Phi = (\phi_1, \phi_2, \phi_3, \phi_4)$ where each ϕ_μ is the WL flux modulo 2π .

The results of applying this framework to (i) the isotropic square-kagome model, (ii) the minimal DM perturbation test, and (iii) the compound-specific Hamiltonian (including the J_{10} -tuning analysis and the impact of symmetry-allowed DM vectors) are presented in Sec. IV.

IV. RESULTS OF SBMFT CALCULATIONS

A. Isotropic square-kagome model: competing SBMFT saddle points and their signatures

We first benchmark our generalized Schwinger-boson mean-field framework on the *isotropic* square-kagome Heisenberg antiferromagnet, where the theoretical expectation is the existence of several nearby competing phases (ordered and quantum-disordered) within the same lattice geometry [3, 4, 7, 9, 11, 13, 32, 41]. We solve the self-consistent

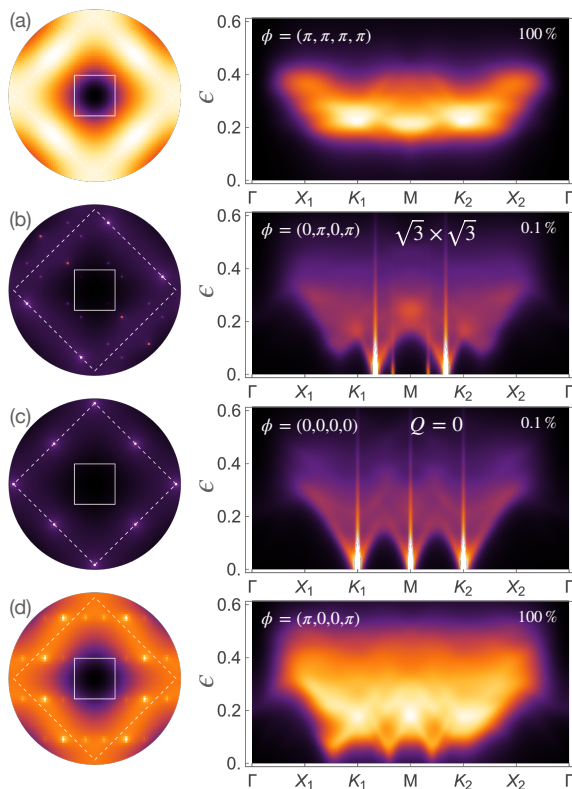


FIG. 5. Equal-time (left) and dynamical (right) spin structure factors obtained within SBMFT for the four lowest-energy Ansätze of the isotropic square-kagome model at $S = 0.3$ without Dzyaloshinskii–Moriya interactions. Panels (a)–(d) correspond to the Wilson-loop flux patterns $\Phi = (\pi, \pi, \pi, \pi)$, $(0, \pi, 0, \pi)$, $(0, 0, 0, 0)$, and $(\pi, 0, 0, \pi)$, identified respectively as a gapped quantum spin liquid, the $\sqrt{3} \times \sqrt{3}$ order, the $Q = 0$ order, and a second gapped quantum spin liquid. The percentage of the total spectral weight displayed is indicated in the plots. The first (solid line) and extended (dashed line) Brillouin zones of the square-kagome lattice showing the location of the Bragg peaks with the fraction of the total spectral weight of the classical (a) $Q = 0$ order, at $(4\pi, 0)$ and $(2\pi, 2\pi)$ [and symmetry related points] with equal spectral weight, and (b) $\sqrt{3} \times \sqrt{3}$ order, at $(2\pi \pm q, 2\pi \mp q)$ with $q = 4\pi/3$, and leading subdominant peaks at $(q, -q)$ with 36%, i. e., $\lambda/\Lambda = 0.36$, of the spectral weight of the dominant ones [47]. The $\sqrt{3} \times \sqrt{3}$ order breaks the four-fold rotational symmetry.

SBMFT equations by tuning the effective spin parameter $\kappa = 2S$. The physical value for the square-kagome lattice corresponds to $S(\sqrt{3} - 1)/2 \simeq 0.366$, which restores the equal-time structure-factor sum rule within SBMFT [41]. As commonly done in SBMFT studies of frustrated magnets, we slightly reduce the effective spin in order to enhance quantum fluctuations and stabilize gapped mean-field solutions, allowing the parent quantum spin-liquid Ansätze to be identified unambiguously. In the following we therefore use $\kappa = 0.6$ (i.e., $S = 0.3$).

At this value, four distinct low-energy self-consistent solutions are obtained, which can be unambiguously classified by their gauge-invariant Wilson-loop (WL) flux patterns on elementary loops [41, 45, 46]. The WLs discussed in

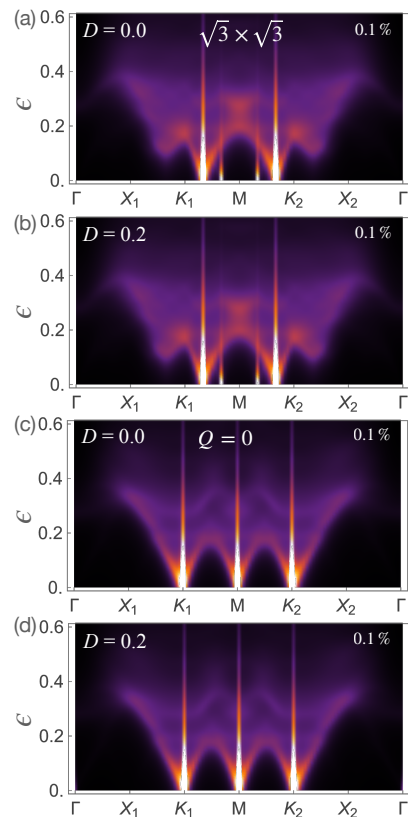


FIG. 6. Dynamical spin structure factor of the isotropic square-kagome model at $S = (\sqrt{3} - 1)/2 \simeq 0.366$. Panels (a,b) show the $\sqrt{3} \times \sqrt{3}$ state and (c,d) the $Q = 0$ state, without and with DM interactions on the J_2 bonds, respectively. The percentage of the total spectral weight displayed is indicated in the plots.

the previous section are defined on elementary six-site loops ($4 \rightarrow 13 \rightarrow 6 \rightarrow 7 \rightarrow 11 \rightarrow 9 \rightarrow 4$) of Fig. 3. Each unit cell admits four symmetry-inequivalent orientations of such loops. The four competing saddle points are characterized by

$$\Phi = (\pi, \pi, \pi, \pi), (0, \pi, 0, \pi), (0, 0, 0, 0), (\pi, 0, 0, \pi). \quad (13)$$

The corresponding equal-time and dynamical spin structure factors are shown in Fig. 5, providing experimentally relevant fingerprints of each saddle point. For clarity, the spectra are normalized to their total weight; in strongly ordered regimes, where most of the weight condenses at the ordering wave vector, only a fraction of the remaining spectral weight is displayed, as indicated in the plots. This representation highlights the strength of the order, reveals residual spectral features, and facilitates comparison between different system sizes. A key outcome of Fig. 5 is that the four saddle points split into two qualitatively distinct classes: (i) two quantum-disordered solutions with fully gapped spinon spectra and diffuse momentum-space correlations [Fig. 5(a,d)], and (ii) two magnetically ordered solutions signaled, within SBMFT, by pronounced low-energy spectral weight at the ordering wavevectors expected for the $Q = 0$ states and $\sqrt{3} \times \sqrt{3}$ states [48] and sharp features in the equal-time structure factor [49] [Fig. 5(b,c)]. In the present parameter set, the magnet-

ically ordered solutions are energetically favored: the $\sqrt{3}\times\sqrt{3}$ and $Q = 0$ states lie below the gapped saddle points, with the $\sqrt{3}\times\sqrt{3}$ state being the lowest-energy solution in our unrestricted search.

Throughout this work, energies are reported as dimensionless mean-field energies per site, expressed in units of the largest exchange coupling J_2 . For the four Ansätze discussed above, we obtain $\epsilon_{(\pi,\pi,\pi,\pi)} = -0.2251(1)$, $\epsilon_{(0,\pi,0,\pi)} = -0.2315(1)$, $\epsilon_{(0,0,0,0)} = -0.2313(6)$, $\epsilon_{(\pi,0,0,\pi)} = -0.2293(5)$. The two ordered solutions $(0,\pi,0,\pi)$ and $(0,0,0,0)$ are nearly degenerate at this value of κ , which motivates a controlled study of how weak SU(2)-breaking perturbations, such as Dzyaloshinskii–Moriya interactions, affect the ordering tendencies. The same energy convention is used consistently throughout the paper, including in the analysis of the dynamical structure factors.

B. Minimal DM perturbation test: DM on J_2 bonds preserves the qualitative hierarchy

To isolate the *intrinsic* role of DM interactions in the square–kagome geometry before turning to the compound-specific Hamiltonian, we perform a minimal diagnostic in which DM terms are applied only on the J_2 bonds of the isotropic model. This choice is not meant to represent a specific material; rather, it is designed as a clean perturbation that (i) explicitly breaks SU(2), (ii) activates triplet hopping/pairing channels in the generalized SBMFT decoupling, and (iii) tests the stability of the competing low-energy saddle points against anisotropy.

For this minimal DM test, we now work at the effective spin parameter $S = (\sqrt{3} - 1)/2 \simeq 0.366$ mentioned earlier. Figure 6 shows the dynamical structure factor for the two low-energy ordered solutions ($\sqrt{3}\times\sqrt{3}$ and $Q = 0$) without DM ($D/J = 0$) and with a representative anisotropy ($D/J = 0.2$). Two robust observations follow: (i) Introducing DM on the J_2 bonds does *not* generate any new competing phase within the explored window: the momentum-space structure of correlations remains qualitatively unchanged. (ii) DM slightly strengthens ordering tendencies (as visible in the enhanced low-energy spectral weight at the same ordering wavevectors), and the energetic splitting remains small but the hierarchy is preserved: for $D/J = 0.2$ the dimensionless energies per site shift from $\epsilon_{\sqrt{3}\times\sqrt{3}} = -0.3104(5)$ and $\epsilon_{Q=0} = -0.3102(4)$ to $\epsilon_{\sqrt{3}\times\sqrt{3}} = -0.3135(2)$ and $\epsilon_{Q=0} = -0.3133(3)$, confirming that weak-to-moderate DM anisotropy does not qualitatively reorder the competition in this minimal setting. This *robustness check* is important because it establishes that the dramatic DM effects discussed below for the realistic Hamiltonian arise from the combined influence of lattice decoration, exchange hierarchy (notably J_{10}), and the full symmetry-allowed DM pattern, rather than from a fragile instability of the isotropic square–kagome SBMFT solutions.

C. Realistic Hamiltonian for $\text{Na}_6\text{Cu}_7\text{BiO}_4(\text{PO}_4)_4\text{Cl}_3$: DM vectors and the central role of J_{10}

We now turn to the compound-specific Hamiltonian for $\text{Na}_6\text{Cu}_7\text{BiO}_4(\text{PO}_4)_4\text{Cl}_3$, where the square–kagome network formed by Cu(1) and Cu(2) is decorated by Cu(3) sites in a checkerboard fashion. From the DFT-based analysis, the dominant isotropic exchanges are J_1 and J_2 on the square–kagome backbone, with additional frustrating diagonal and longer-range couplings (including J_3 and J_4) and, crucially, a sizeable coupling J_{10} connecting the decorating Cu(3) sites to the backbone (Table I and Fig. 3). The J_{10} coupling controls the degree of hybridization between the decorating sublattice and the frustrated backbone. The symmetry-allowed DM vectors are extracted from spin-orbit-coupled Wannier-based hopping matrices and summarized (one representative per symmetry class) in Table IV. Their magnitudes reach ~ 10 – 30 K on the leading exchange pathways, making them a potentially relevant perturbation on the energy scales of interest.

Within SBMFT, J_{10} emerges as an efficient control parameter for the proximity to boson condensation (magnetic order). To quantify this statement we compute the minimum spinon gap Δ_{spinon} as a function of J_{10}/J_2 for the realistic exchange parameters of Ref. [32] at fixed $S = 0.125$ (chosen to stabilize gapped solutions and enable controlled tracking of softening trends). Fig. 7 shows $\Delta_{\text{spinon}}(J_{10})$ for two cluster sizes $N = 1008$ and 4032 (respectively $l = 6$ and 12), together with a thermodynamic-limit extrapolation obtained from finite-size scaling.

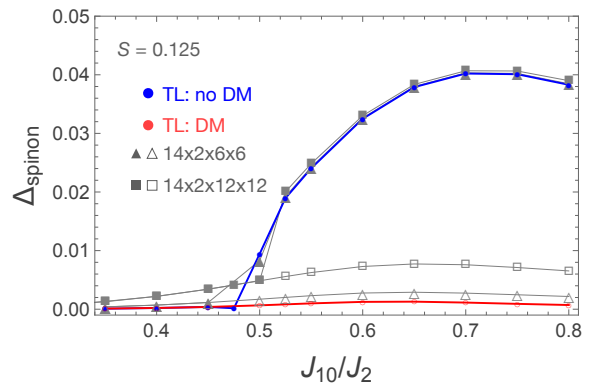


FIG. 7. Minimum spinon gap Δ_{spinon} as a function of J_{10}/J_2 for the realistic exchange parameters of Ref. [32] at $S = 0.125$. Open and filled symbols denote calculations without and with DM interactions, respectively, for finite clusters of size $N = 1008$ (triangles) and $N = 4032$ (squares). Blue and red circles indicate the corresponding thermodynamic-limit estimates obtained from finite-size scaling. Reducing J_{10} suppresses the spinon gap, while DM interactions shift the system further toward condensation.

Three strong conclusions follow directly from Fig. 7:

- (i) J_{10} stabilizes the gapped regime. Reducing J_{10} suppresses Δ_{spinon} continuously, driving the system toward a condensation threshold within SBMFT.
- (ii) DM promotes condensation. Including the full

symmetry-allowed DM pattern shifts the gap downward relative to the $D = 0$ case for the same J_{10} , indicating that spin-orbit-induced anisotropy enhances the tendency toward magnetic ordering in the realistic model.

(iii) The trend is not a finite-size artifact. The finite-size data at $N = 1008$ and $N = 4032$ exhibit a consistent systematic evolution, and the extrapolated thermodynamic-limit curves retain the same qualitative separation between the $D = 0$ and $D \neq 0$ cases, supporting the robustness of the conclusion that J_{10} tunes the system through a near-critical regime and that DM shifts the instability toward larger J_{10} .

D. Spectral fingerprints: illustrative vs realistic J_{10} and the effect of DM

To connect the gap evolution to experimentally relevant correlation functions, we compute both equal-time and dynamical spin structure factors for two representative regimes (Fig. 8).

The illustrative regime uses an artificially large $J_{10} = 150$ K and therefore provides a controlled reference deep in the gapped, quantum-disordered side of the SBMFT solutions. In this regime, both the equal-time maps and the dynamical response exhibit a clear finite-energy onset and broad momentum-space features consistent with a stable gapped spectrum.

The realistic regime uses the compound parameter $J_{10} = 64.6$ K (as in Ref. [32]) and reveals the main qualitative change: spectral weight is transferred toward low energies at specific momenta, signaling pronounced soft-mode formation. Importantly, adding the symmetry-allowed DM vectors (taken from Table IV) further enhances this low-energy transfer, consistent with the DM-driven downward shift of Δ_{spinon} seen in Fig. 7. Taken together, Figs. 7–8 establish a coherent picture: J_{10} controls the stability of the gapped regime, and DM interactions enhance the instability toward condensation in the realistic decorated square–kagome Hamiltonian.

A noteworthy aspect of the realistic spectra is that none of the four flux states stabilized in the isotropic square–kagome benchmark appears to describe the compound Hamiltonian in a simple way. Instead, the location of the soft modes and the redistribution of spectral weight point to a more complex ordering tendency in the decorated model, consistent with the additional Cu(3) sublattice and the dominant exchange scales.

E. Alternative exchange set and proximity to SBMFT condensation

Finally, we repeat the analysis for the alternative exchange parameters obtained for $U = 6.66$ eV (Table I), using $S = 0.115$ and comparing illustrative and realistic regimes with and without DM and on a cluster of $N = 4032$ sites (Fig. 9). In this parameter set, J_{10} is smaller, placing the system even closer to the condensation boundary. As a result, including DM interactions makes self-consistency increasingly demanding near the physical J_{10} : the iterative cycle tends to drive

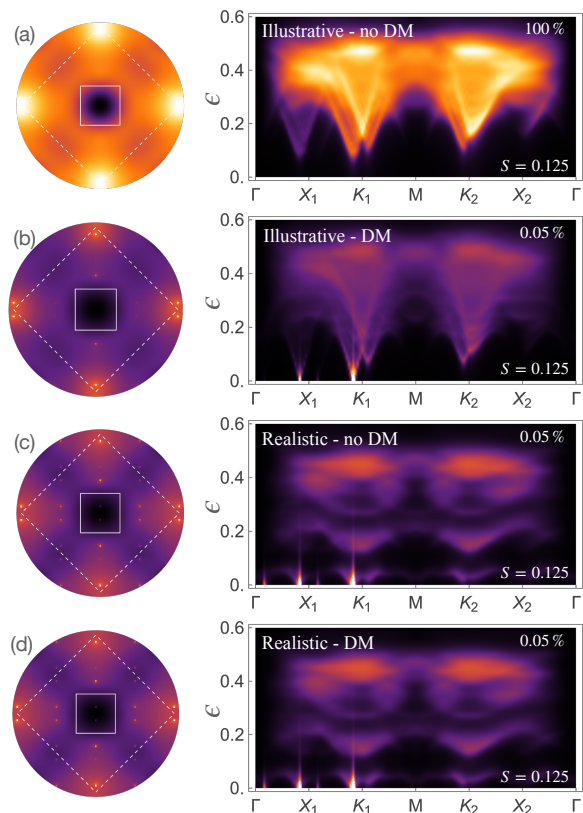


FIG. 8. Equal-time (left) and dynamical (right) spin structure factors for the DFT-derived exchange parameters of Ref. [32] at $S = 0.125$. Panels (a,b) show an illustrative gapped regime with $J_{10} = 150$ K, without and with DM interactions, respectively; panels (c,d) show the realistic regime with $J_{10} = 64.6$ K as calculated in Ref. [32]), again without and with DM. DM vectors are taken from Table IV. Lowering J_{10} transfers spectral weight to low energies, a tendency further enhanced by the symmetry-allowed DM interactions. The percentage of the total spectral weight shown in each panel is indicated in the plots.

the solution toward condensation, and convergence can fail in the immediate vicinity of the physical parameter set. Nevertheless, convergence is achieved for slightly larger J_{10} , and the *smooth evolution* of the converged solutions toward the physical regime supports a physically controlled interpretation: the lack of convergence is not evidence of an uncontrolled numerical artifact, but rather is consistent with the expected breakdown of a gapped SBMFT saddle point as the system approaches boson condensation (magnetic ordering) in the thermodynamic limit.

V. DISCUSSION AND OUTLOOK

We have investigated the role of Dzyaloshinskii–Moriya (DM) interactions in square-kagome quantum antiferromagnets by combining *ab initio* extraction of symmetry-allowed DM vectors for $\text{Na}_6\text{Cu}_7\text{BiO}_4(\text{PO}_4)_4\text{Cl}_3$ with a generalized Schwinger-boson self-consistent mean-field treatment that re-

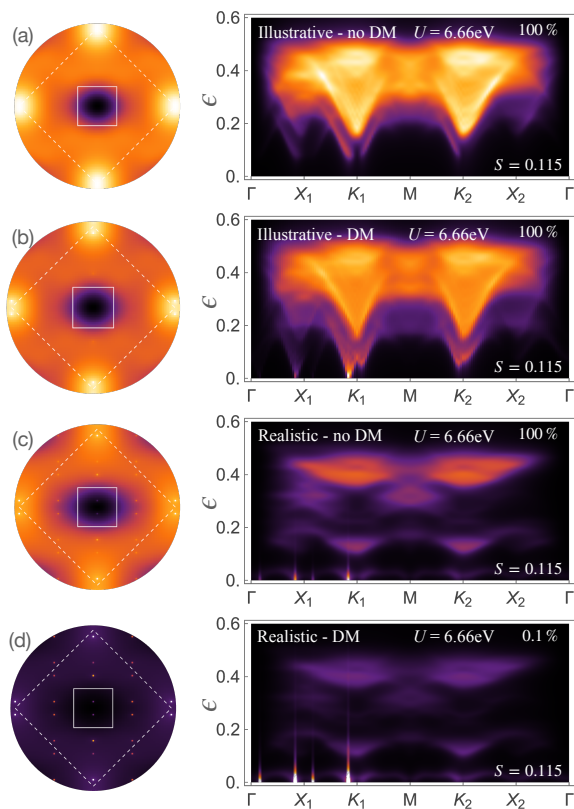


FIG. 9. Equal-time (left) and dynamical (right) spin structure factors for the exchange parameters obtained at $U = 6.66$ eV, evaluated at $S = 0.115$. Panels (a,b) show an illustrative regime with an arbitrarily large J_{10} , without and with DM interactions, respectively; panels (c,d) show the realistic regime with $J_{10} = 64.6$ K, again without and with DM. DM vectors are taken from Table IV. The enhanced low-energy spectral weight indicates that this parameter set lies closer to magnetic condensation. The percentage of the total spectral weight displayed in each panel is indicated in the plots.

tains both singlet and triplet hopping/pairing channels. This combination allows us to address, within a single framework, both the generic effect of anisotropy on the square-kagome geometry and its material-specific impact in a decorated square-kagome compound.

At the level of the isotropic square-kagome benchmark, we identified several competing low-energy SBMFT saddle points distinguished by their Wilson-loop fluxes and by clear equal-time and dynamical structure-factor fingerprints. A minimal DM perturbation restricted to the J_2 bonds does not qualitatively reshape this competing landscape, but it already enhances ordering tendencies, indicating that anisotropy acts in a systematic rather than accidental way in this geometry.

For the realistic compound Hamiltonian of $\text{Na}_6\text{Cu}_7\text{BiO}_4(\text{PO}_4)_4\text{Cl}_3$, a clearer physical picture can be established. The coupling J_{10} , which links the decorating Cu(3) sites to the square-kagome backbone, acts as the control parameter stabilizing the gapped quantum-paramagnetic regime. Reducing J_{10} continuously suppresses the minimum spinon gap, while the full symmetry-allowed DM pattern shifts the system further toward boson condensation. In this

sense, decorated square-kagome antiferromagnets exhibit a simple but important control knob: J_{10} stabilizes the quantum-paramagnetic regime, whereas symmetry-allowed DM interactions systematically destabilize it and drive the system toward magnetic condensation.

This places $\text{Na}_6\text{Cu}_7\text{BiO}_4(\text{PO}_4)_4\text{Cl}_3$ in close proximity to a magnetic instability. Our results therefore refine the picture of this compound from that of a merely robust quantum paramagnet to that of a material located near the boundary between a gapped disordered regime and anisotropy-enhanced ordering. More broadly, our results show that decorated square-kagome materials are not simply Heisenberg-frustrated magnets, but systems in which spin-orbit anisotropy provides a quantitatively relevant tuning field.

The present work also suggests several experimental directions. Since the leading DM terms enhance low-energy soft modes and redistribute spectral weight in momentum space, anisotropy-sensitive probes such as NMR and direction-dependent susceptibility measurements should be particularly informative. ESR may also be useful provided that the relevant low-energy anisotropy scale lies within the experimentally accessible frequency window. If momentum-resolved spectroscopy becomes available, the predicted buildup of low-energy spectral weight at specific wave vectors would provide a direct test of the proximity to condensation identified here. On the theory side, it will be important to complement the present SBMFT analysis with approaches that treat the onset of order beyond mean field and can further clarify the nature of the instability in the immediate vicinity of the physical parameter regime.

Overall, our results establish DM interactions as a central ingredient of square-kagome quantum magnetism in realistic low-symmetry materials. In doing so, they identify a general instability mechanism for decorated square-kagome antiferromagnets and provide a microscopic framework for interpreting the growing family of square-kagome and related materials.

ACKNOWLEDGEMENTS

We thank Harald O. Jeschke and Alexander N. Vasiliev for helpful discussions.

The work Y.I. was performed in part at the Aspen Center for Physics, which is supported by a grant from the Simons Foundation (1161654, Troyer). This research was also supported in part by grant NSF PHY-2309135 to the Kavli Institute for Theoretical Physics and by the International Centre for Theoretical Sciences (ICTS) for participating in the Discussion Meeting - Fractionalized Quantum Matter (code: ICTS/DMFQM2025/07). Y.I. acknowledges support from the Abdus Salam International Centre for Theoretical Physics through the Associates Programme, from the Simons Foundation through Grant No. 284558FY19, from IIT Madras through the Institute of Eminence program for establishing QuCenDiEM (Project No. SP22231244CPETWOQCDHOC). S.S. and A.R. thank IIT Madras for a Visiting Faculty Fellow position under the IoE

program during which this project was initiated. A.R. acknowledges support from the french national agency (ANR FlatMoi, grant no. ANR-21-CE30-0029). L.T. and S.S. acknowledge support of the Ministry of Science and Higher Education of the Russian Federation through the IMP UB RAS. The work of VVM was supported by the Ministry of Science and Higher Education of the Russian Federation (Grant No. FEUZ-2026-0010).

APPENDIX A: Electronic structure

The electronic structure obtained within the GGA calculations is presented in the form of the total and orbital-resolved density of states of $\text{Na}_6\text{Cu}_7\text{BiO}_4(\text{PO}_4)_4\text{Cl}_3$, complementing the band-structure evidence for the isolated Cu $d_{x^2-y^2}$ -derived manifold discussed in Sec. II. The energy range from -7.8 eV to -3.6 eV below the Fermi level is predominantly occupied by O- p states hybridized with Cu- d , P- p , and Cl- p orbitals. From -3.6 eV to 0.7 eV, Cu- d states dominate, hybridizing with O- p and Cl- p states. An energy gap is observed at approximately from -1 to -0.6 eV relative to E_F . The strongest peaks in the partial Cu- d DOS appear at -2.0 eV and -1.3 eV, corresponding to fully filled xz/yz , $3z^2 - r^2$, and xy orbitals, as well as the half-filled $x^2 - y^2$ orbital. The unoccupied $x^2 - y^2$ states are located between -0.6 eV and 0.6 eV.

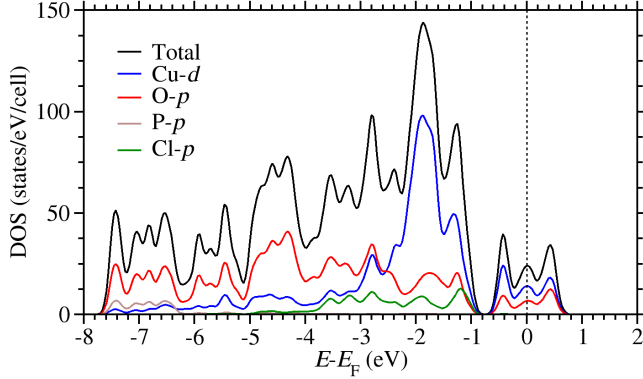


FIG. 10. Total and orbital-resolved density of states of $\text{Na}_6\text{Cu}_7\text{BiO}_4(\text{PO}_4)_4\text{Cl}_3$ from nonmagnetic GGA calculations. The black curve shows the total density of states, while the colored curves show the partial contributions from Cu- d , O- p , P- p , and Cl- p states. The Fermi energy is set to zero. The low-energy unoccupied manifold is dominated by Cu $d_{x^2-y^2}$ character, consistent with the employed one-band description.

APPENDIX B: Isotropic and antisymmetric anisotropic exchange interactions

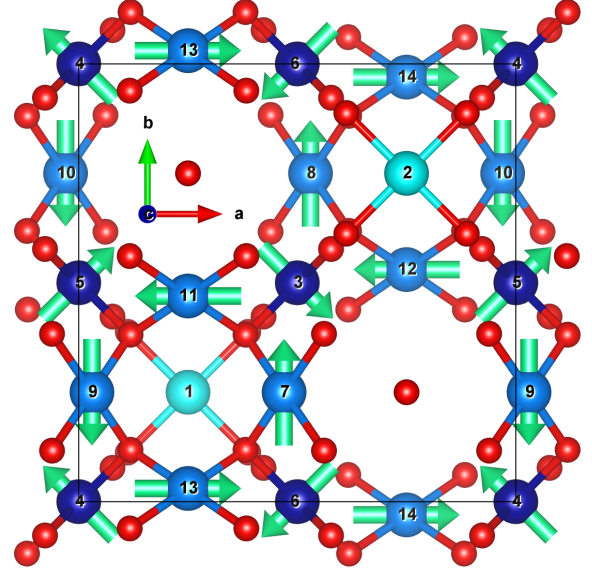


FIG. 11. Total DM interaction vectors (green arrows) for all Cu sites in $\text{Na}_6\text{Cu}_7\text{BiO}_4(\text{PO}_4)_4\text{Cl}_3$. The arrows indicate the site-resolved sums of the bond DM vectors connected to each Cu site, shown here in the crystallographic geometry of the unit cell. The resulting pattern summarizes the local anisotropic environment that constrains the symmetry-allowed canting tendencies of the Cu moments.

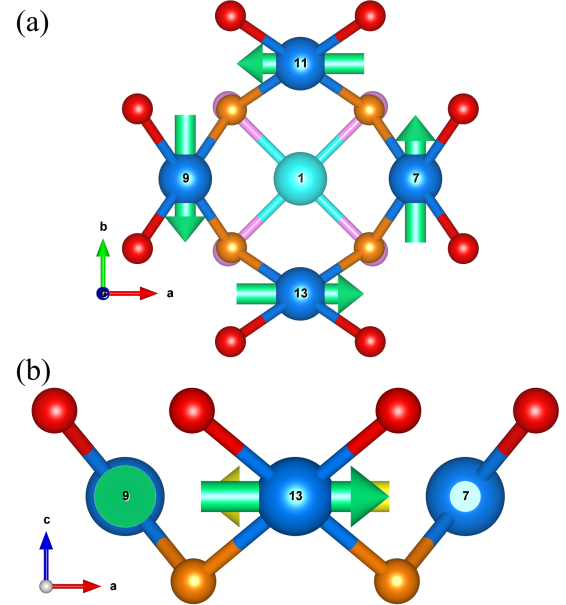


FIG. 12. Total DM interaction vectors (green arrows) for Cu(2) sites in $\text{Na}_6\text{Cu}_7\text{BiO}_4(\text{PO}_4)_4\text{Cl}_3$ viewed along the (a) c -axis (ab -plane) and (b) b -axis (ac -plane). Red, orange, and pink spheres denote oxygen atoms at distinct heights along the c -axis.

TABLE III: Complete set of isotropic exchange interactions J_n (in K) and corresponding Cu–Cu bond distances (in Å) for $\text{Na}_6\text{Cu}_7\text{BiO}_4(\text{PO}_4)_4\text{Cl}_3$, evaluated for $U = 6.66, 7, \text{ and } 8$ eV. The dominant exchange paths discussed are labeled in Fig. 3. This table extends Table I by listing the full hierarchy of exchange couplings, including weaker longer-range terms.

U (eV)	J_1 (K)	J_2	J_3	J_4	J_5	J_6	J_7	J_8	J_9	J_{10}
6.66	157.7	202.8	87.3	29.4	9.0	0.2	0.0	1.1	3.9	47.8
7	150.0	193.0	83.0	27.9	8.6	0.2	0.0	1.0	3.7	45.5
8	131.3	168.8	72.7	24.4	7.5	0.2	0.0	0.9	3.3	39.8
d (Å)	3.114	3.278	4.404	5.009	5.266	5.340	5.614	5.727	5.769	6.018
U (eV)	J_{11}	J_{12}	J_{13}	J_{14}	J_{15}	J_{16}	J_{17}	J_{18}	J_{19}	J_{20}
6.66	0.4	0.1	1.7	5.0	0.1	0.0	0.3	0.0	0.0	0.1
7	0.3	0.1	1.6	4.8	0.1	0.0	0.3	0.0	0.0	0.1
8	0.3	0.1	1.4	4.2	0.1	0.0	0.2	0.0	0.0	0.1
d (Å)	6.234	6.381	6.555	7.084	7.717	7.761	7.805	7.807	8.120	8.228

TABLE IV: Complete set of Dzyaloshinskii–Moriya vectors \mathbf{D}_{mn} (in K) for $\text{Na}_6\text{Cu}_7\text{BiO}_4(\text{PO}_4)_4\text{Cl}_3$ at $U = 6.66$ eV. For each Cu–Cu bond, the table lists the bond distance, bond label, bond vector \mathbf{R}_{mn} , and the corresponding DM vector \mathbf{D}_{mn} . The Cu-site labels refer to Fig. 3. This table provides the full symmetry-resolved DM dataset underlying the representative values summarized in Table II.

d (Å)	Bond m-n	\mathbf{R}_{mn}	\mathbf{D}_{mn} (K)	d (Å)	Bond m-n	\mathbf{R}_{mn}	\mathbf{D}_{mn} (K)
3.114	Cu7-Cu11	(-2.2 ; 2.2 ; 0.0)	(5.8 ; 5.8 ; -11.2)	6.018	Cu1-Cu8	(2.8 ; 5.0 ; 1.8)	(0.9 ; 1.7 ; 2.8)
3.114	Cu13-Cu7	(2.2 ; 2.2 ; 0.0)	(5.8 ; -5.8 ; -11.2)	6.018	Cu1-Cu12	(5.0 ; 2.8 ; 1.8)	(-1.7 ; -0.9 ; -2.8)
3.114	Cu9-Cu13	(2.2 ; -2.2 ; 0.0)	(-5.8 ; -5.8 ; -11.2)	6.018	Cu1-Cu10	(-2.8 ; 5.0 ; 1.8)	(0.9 ; -1.7 ; -2.8)
3.114	Cu11-Cu9	(-2.2 ; -2.2 ; 0.0)	(-5.8 ; 5.8 ; -11.2)	6.018	Cu1-Cu14	(5.0 ; -2.8 ; 1.8)	(1.7 ; -0.9 ; 2.8)
3.114	Cu8-Cu12	(2.2 ; -2.2 ; 0.0)	(5.8 ; 5.8 ; -11.2)	6.234	Cu7-Cu4	(5.3 ; -2.5 ; -2.1)	(0.0 ; -0.1 ; 0.0)
3.114	Cu14-Cu8	(-2.2 ; -2.2 ; 0.0)	(5.8 ; -5.8 ; -11.2)	6.234	Cu7-Cu5	(5.3 ; 2.5 ; -2.1)	(0.0 ; -0.1 ; 0.0)
3.114	Cu10-Cu14	(-2.2 ; 2.2 ; 0.0)	(-5.8 ; -5.8 ; -11.2)	6.234	Cu14-Cu5	(2.5 ; 5.3 ; 2.1)	(-0.1 ; 0.0 ; 0.0)
3.114	Cu12-Cu10	(2.2 ; 2.2 ; 0.0)	(-5.8 ; 5.8 ; -11.2)	6.234	Cu14-Cu3	(-2.5 ; 5.3 ; 2.1)	(-0.1 ; 0.0 ; 0.0)
3.278	Cu3-Cu11	(-2.5 ; -0.3 ; 2.1)	(7.3 ; -19.1 ; -18.8)	6.234	Cu9-Cu3	(-5.3 ; 2.5 ; -2.1)	(0.0 ; 0.1 ; 0.0)
3.278	Cu7-Cu3	(-0.3 ; -2.5 ; 2.1)	(-19.1 ; 7.3 ; -18.8)	6.234	Cu9-Cu6	(-5.3 ; -2.5 ; -2.1)	(0.0 ; 0.1 ; 0.0)
3.278	Cu11-Cu5	(2.5 ; -0.3 ; 2.1)	(-7.3 ; -19.1 ; -18.8)	6.234	Cu12-Cu6	(-2.5 ; -5.3 ; 2.1)	(0.1 ; 0.0 ; 0.0)
3.278	Cu5-Cu9	(0.3 ; -2.5 ; 2.1)	(19.1 ; 7.3 ; -18.8)	6.234	Cu12-Cu4	(2.5 ; -5.3 ; 2.1)	(0.1 ; 0.0 ; 0.0)
3.278	Cu9-Cu4	(0.3 ; 2.5 ; 2.1)	(19.1 ; -7.3 ; -18.8)	6.234	Cu11-Cu6	(2.5 ; 5.3 ; -2.1)	(0.1 ; 0.0 ; 0.0)
3.278	Cu4-Cu13	(2.5 ; 0.3 ; 2.1)	(-7.3 ; 19.1 ; -18.8)	6.234	Cu11-Cu4	(-2.5 ; 5.3 ; -2.1)	(0.1 ; 0.0 ; 0.0)
3.278	Cu13-Cu6	(-2.5 ; 0.3 ; 2.1)	(7.3 ; 19.1 ; -18.8)	6.234	Cu8-Cu4	(-5.3 ; 2.5 ; 2.1)	(0.0 ; -0.1 ; 0.0)
3.278	Cu6-Cu7	(-0.3 ; 2.5 ; 2.1)	(-19.1 ; -7.3 ; -18.8)	6.234	Cu8-Cu5	(-5.3 ; -2.5 ; 2.1)	(0.0 ; -0.1 ; 0.0)
3.278	Cu8-Cu3	(0.3 ; 2.5 ; -2.1)	(-19.1 ; 7.3 ; -18.8)	6.234	Cu5-Cu13	(2.5 ; 5.3 ; 2.1)	(0.1 ; 0.0 ; 0.0)
3.278	Cu3-Cu12	(2.5 ; 0.3 ; -2.1)	(7.3 ; -19.1 ; -18.8)	6.234	Cu3-Cu13	(-2.5 ; 5.3 ; 2.1)	(0.1 ; 0.0 ; 0.0)
3.278	Cu12-Cu5	(-2.5 ; 0.3 ; -2.1)	(-7.3 ; -19.1 ; -18.8)	6.234	Cu10-Cu3	(5.3 ; -2.5 ; 2.1)	(0.0 ; 0.1 ; 0.0)
3.278	Cu5-Cu10	(-0.3 ; 2.5 ; -2.1)	(19.1 ; 7.3 ; -18.8)	6.234	Cu10-Cu6	(5.3 ; 2.5 ; 2.1)	(0.0 ; 0.1 ; 0.0)
3.278	Cu10-Cu4	(-0.3 ; -2.5 ; -2.1)	(19.1 ; -7.3 ; -18.8)	6.381	Cu1-Cu7	(2.2 ; 0.0 ; 6.0)	(0.0 ; 0.0 ; 0.0)
3.278	Cu4-Cu14	(-2.5 ; -0.3 ; -2.1)	(-7.3 ; 19.1 ; -18.8)	6.381	Cu1-Cu11	(0.0 ; 2.2 ; 6.0)	(0.0 ; 0.0 ; 0.0)
3.278	Cu14-Cu6	(2.5 ; -0.3 ; -2.1)	(7.3 ; 19.1 ; -18.8)	6.381	Cu1-Cu9	(-2.2 ; 0.0 ; 6.0)	(0.0 ; 0.0 ; 0.0)
3.278	Cu6-Cu8	(0.3 ; -2.5 ; -2.1)	(-19.1 ; -7.3 ; -18.8)	6.381	Cu1-Cu13	(0.0 ; -2.2 ; 6.0)	(0.0 ; 0.0 ; 0.0)
4.404	Cu11-Cu13	(0.0 ; -4.4 ; 0.0)	(8.9 ; 0.0 ; 0.0)	6.381	Cu2-Cu8	(-2.2 ; 0.0 ; -6.0)	(0.0 ; 0.0 ; 0.0)
4.404	Cu9-Cu7	(4.4 ; 0.0 ; 0.0)	(0.0 ; 8.9 ; 0.0)	6.381	Cu2-Cu10	(2.2 ; 0.0 ; -6.0)	(0.0 ; 0.0 ; 0.0)
4.404	Cu12-Cu14	(0.0 ; 4.4 ; 0.0)	(8.9 ; 0.0 ; 0.0)	6.381	Cu2-Cu12	(0.0 ; -2.2 ; -6.0)	(0.0 ; 0.0 ; 0.0)
4.404	Cu10-Cu8	(-4.4 ; 0.0 ; 0.0)	(0.0 ; 8.9 ; 0.0)	6.381	Cu2-Cu14	(0.0 ; 2.2 ; -6.0)	(0.0 ; 0.0 ; 0.0)
5.009	Cu3-Cu5	(-5.0 ; 0.0 ; 0.0)	(0.0 ; -10.8 ; 1.9)	6.555	Cu9-Cu10	(-0.6 ; 5.0 ; -4.2)	(0.0 ; 0.0 ; 0.0)
5.009	Cu5-Cu4	(0.0 ; -5.0 ; 0.0)	(10.8 ; 0.0 ; 1.9)	6.555	Cu13-Cu14	(5.0 ; -0.6 ; -4.2)	(0.0 ; 0.0 ; 0.0)
5.009	Cu4-Cu6	(5.0 ; 0.0 ; 0.0)	(0.0 ; 10.8 ; 1.9)	6.555	Cu7-Cu8	(0.6 ; 5.0 ; -4.2)	(0.0 ; 0.0 ; 0.0)
5.009	Cu6-Cu3	(0.0 ; 5.0 ; 0.0)	(-10.8 ; 0.0 ; 1.9)	6.555	Cu11-Cu12	(5.0 ; 0.6 ; -4.2)	(0.0 ; 0.0 ; 0.0)
5.266	Cu1-Cu4	(-2.5 ; -2.5 ; 3.9)	(1.3 ; -1.3 ; 0.0)	7.084	Cu4-Cu3	(5.0 ; 5.0 ; 0.0)	(-1.9 ; 1.9 ; 0.0)
5.266	Cu1-Cu3	(2.5 ; 2.5 ; 3.9)	(-1.3 ; 1.3 ; 0.0)	7.084	Cu6-Cu5	(-5.0 ; 5.0 ; 0.0)	(-1.9 ; -1.9 ; 0.0)
5.266	Cu1-Cu5	(-2.5 ; 2.5 ; 3.9)	(-1.3 ; -1.3 ; 0.0)	7.717	Cu1-Cu2	(5.0 ; 5.0 ; -3.1)	(0.0 ; 0.0 ; 0.0)
5.266	Cu1-Cu6	(2.5 ; -2.5 ; 3.9)	(1.3 ; 1.3 ; 0.0)	7.761	Cu11-Cu8	(2.8 ; 2.8 ; 6.7)	(0.0 ; 0.0 ; 0.0)
5.266	Cu2-Cu3	(-2.5 ; -2.5 ; -3.9)	(-1.3 ; 1.3 ; 0.0)	7.761	Cu11-Cu10	(-2.8 ; 2.8 ; 6.7)	(0.0 ; 0.0 ; 0.0)

Continued on next page

TABLE IV: (continued)

d (Å)	Bond m-n	\mathbf{R}_{mn}	\mathbf{D}_{mn}	d (Å)	Bond m-n	\mathbf{R}_{mn}	\mathbf{D}_{mn}
5.266	Cu2-Cu5	(2.5; -2.5; -3.9)	(-1.3; -1.3; 0.0)	7.761	Cu13-Cu8	(2.8; -2.8; 6.7)	(0.0; 0.0; 0.0)
5.266	Cu2-Cu6	(-2.5; 2.5; -3.9)	(1.3; 1.3; 0.0)	7.761	Cu13-Cu10	(-2.8; -2.8; 6.7)	(0.0; 0.0; 0.0)
5.266	Cu2-Cu4	(2.5; 2.5; -3.9)	(1.3; -1.3; 0.0)	7.761	Cu7-Cu12	(2.8; 2.8; 6.7)	(0.0; 0.0; 0.0)
5.340	Cu1-Cu7	(2.2; 0.0; -4.9)	(0.0; 0.0; 0.0)	7.761	Cu7-Cu14	(2.8; -2.8; 6.7)	(0.0; 0.0; 0.0)
5.340	Cu1-Cu9	(-2.2; 0.0; -4.9)	(0.0; 0.0; 0.0)	7.761	Cu9-Cu12	(-2.8; 2.8; 6.7)	(0.0; 0.0; 0.0)
5.340	Cu1-Cu11	(0.0; 2.2; -4.9)	(0.0; 0.0; 0.0)	7.761	Cu9-Cu14	(-2.8; -2.8; 6.7)	(0.0; 0.0; 0.0)
5.340	Cu1-Cu13	(0.0; -2.2; -4.9)	(0.0; 0.0; 0.0)	7.805	Cu4-Cu14	(7.5; -0.3; -2.1)	(0.0; 0.1; 0.0)
5.340	Cu2-Cu8	(-2.2; 0.0; 4.9)	(0.0; 0.0; 0.0)	7.805	Cu4-Cu10	(-0.3; 7.5; -2.1)	(-0.1; 0.0; 0.0)
5.340	Cu2-Cu10	(2.2; 0.0; 4.9)	(0.0; 0.0; 0.0)	7.805	Cu4-Cu13	(-7.5; 0.3; 2.1)	(0.0; 0.1; 0.0)
5.340	Cu2-Cu12	(0.0; -2.2; 4.9)	(0.0; 0.0; 0.0)	7.805	Cu4-Cu9	(0.3; -7.5; 2.1)	(-0.1; 0.0; 0.0)
5.340	Cu2-Cu14	(0.0; 2.2; 4.9)	(0.0; 0.0; 0.0)	7.805	Cu6-Cu8	(0.3; 7.5; -2.1)	(-0.1; 0.0; 0.0)
5.614	Cu11-Cu13	(0.0; 5.6; 0.0)	(0.0; 0.0; 0.0)	7.805	Cu6-Cu13	(7.5; 0.3; 2.1)	(0.0; -0.1; 0.0)
5.614	Cu12-Cu14	(0.0; -5.6; 0.0)	(0.0; 0.0; 0.0)	7.805	Cu6-Cu14	(-7.5; -0.3; -2.1)	(0.0; -0.1; 0.0)
5.614	Cu8-Cu10	(-5.6; 0.0; 0.0)	(0.0; 0.0; 0.0)	7.805	Cu6-Cu7	(-0.3; -7.5; 2.1)	(-0.1; 0.0; 0.0)
5.614	Cu7-Cu9	(5.6; 0.0; 0.0)	(0.0; 0.0; 0.0)	7.805	Cu3-Cu11	(7.5; -0.3; 2.1)	(0.0; -0.1; 0.0)
5.727	Cu9-Cu6	(4.7; -2.5; -2.1)	(-0.2; 0.6; 0.5)	7.805	Cu3-Cu12	(-7.5; 0.3; -2.1)	(0.0; -0.1; 0.0)
5.727	Cu9-Cu3	(4.7; 2.5; -2.1)	(0.2; 0.6; -0.5)	7.805	Cu3-Cu7	(-0.3; 7.5; 2.1)	(0.1; 0.0; 0.0)
5.727	Cu5-Cu13	(2.5; -4.7; 2.1)	(0.6; -0.2; 0.5)	7.805	Cu3-Cu8	(0.3; -7.5; -2.1)	(0.1; 0.0; 0.0)
5.727	Cu13-Cu3	(2.5; 4.7; -2.1)	(-0.6; -0.2; 0.5)	7.805	Cu5-Cu12	(7.5; 0.3; -2.1)	(0.0; 0.1; 0.0)
5.727	Cu7-Cu4	(-4.7; -2.5; -2.1)	(-0.2; -0.6; -0.5)	7.805	Cu5-Cu11	(-7.5; -0.3; 2.1)	(0.0; 0.1; 0.0)
5.727	Cu7-Cu5	(-4.7; 2.5; -2.1)	(0.2; -0.6; 0.5)	7.805	Cu5-Cu9	(0.3; 7.5; 2.1)	(0.1; 0.0; 0.0)
5.727	Cu11-Cu4	(-2.5; -4.7; -2.1)	(0.6; 0.2; 0.5)	7.805	Cu5-Cu10	(-0.3; -7.5; -2.1)	(0.1; 0.0; 0.0)
5.727	Cu11-Cu6	(2.5; -4.7; -2.1)	(0.6; -0.2; -0.5)	7.807	Cu1-Cu3	(2.5; 2.5; -7.0)	(0.0; 0.0; 0.0)
5.727	Cu8-Cu5	(4.7; -2.5; 2.1)	(0.2; -0.6; 0.5)	7.807	Cu1-Cu4	(-2.5; -2.5; -7.0)	(0.0; 0.0; 0.0)
5.727	Cu8-Cu4	(4.7; 2.5; 2.1)	(-0.2; -0.6; -0.5)	7.807	Cu1-Cu5	(-2.5; 2.5; -7.0)	(0.0; 0.0; 0.0)
5.727	Cu12-Cu4	(2.5; 4.7; 2.1)	(0.6; 0.2; 0.5)	7.807	Cu1-Cu6	(2.5; -2.5; -7.0)	(0.0; 0.0; 0.0)
5.727	Cu12-Cu6	(-2.5; 4.7; 2.1)	(0.6; -0.2; -0.5)	7.807	Cu2-Cu3	(-2.5; -2.5; 7.0)	(0.0; 0.0; 0.0)
5.727	Cu10-Cu3	(-4.7; -2.5; 2.1)	(0.2; 0.6; -0.5)	7.807	Cu2-Cu4	(2.5; 2.5; 7.0)	(0.0; 0.0; 0.0)
5.727	Cu10-Cu6	(-4.7; 2.5; 2.1)	(-0.2; 0.6; 0.5)	7.807	Cu2-Cu5	(2.5; -2.5; 7.0)	(0.0; 0.0; 0.0)
5.727	Cu14-Cu3	(-2.5; -4.7; 2.1)	(-0.6; -0.2; 0.5)	7.807	Cu2-Cu6	(-2.5; 2.5; 7.0)	(0.0; 0.0; 0.0)
5.727	Cu14-Cu5	(2.5; -4.7; 2.1)	(-0.6; 0.2; -0.5)	8.120	Cu7-Cu11	(7.8; 2.2; 0.0)	(0.0; 0.0; 0.0)
5.769	Cu7-Cu14	(2.8; -2.8; -4.2)	(0.1; -0.1; 0.7)	8.120	Cu11-Cu9	(-2.2; 7.8; 0.0)	(0.0; 0.0; 0.0)
5.769	Cu14-Cu9	(2.8; 2.8; 4.2)	(-0.1; -0.1; 0.7)	8.120	Cu9-Cu13	(2.2; 7.8; 0.0)	(0.0; 0.0; 0.0)
5.769	Cu9-Cu12	(-2.8; 2.8; -4.2)	(-0.1; 0.1; 0.7)	8.120	Cu13-Cu7	(2.2; -7.8; 0.0)	(0.0; 0.0; 0.0)
5.769	Cu12-Cu7	(-2.8; -2.8; 4.2)	(0.1; 0.1; 0.7)	8.120	Cu10-Cu14	(7.8; 2.2; 0.0)	(0.0; 0.0; 0.0)
5.769	Cu10-Cu11	(2.8; -2.8; 4.2)	(-0.1; 0.1; 0.7)	8.120	Cu14-Cu8	(-2.2; 7.8; 0.0)	(0.0; 0.0; 0.0)
5.769	Cu11-Cu8	(2.8; 2.8; -4.2)	(0.1; 0.1; 0.7)	8.120	Cu8-Cu12	(-7.8; -2.2; 0.0)	(0.0; 0.0; 0.0)
5.769	Cu8-Cu13	(-2.8; 2.8; 4.2)	(0.1; -0.1; 0.7)	8.120	Cu12-Cu10	(2.2; -7.8; 0.0)	(0.0; 0.0; 0.0)
5.769	Cu13-Cu10	(-2.8; -2.8; -4.2)	(-0.1; -0.1; 0.7)	8.228	Cu8-Cu9	(-5.0; -5.0; 4.2)	(0.0; 0.0; 0.0)
6.018	Cu2-Cu11	(-5.0; -2.8; -1.8)	(-1.7; -0.9; -2.8)	8.228	Cu7-Cu10	(5.0; 5.0; -4.2)	(0.0; 0.0; 0.0)
6.018	Cu2-Cu7	(-2.8; -5.0; -1.8)	(0.9; 1.7; 2.8)	8.228	Cu13-Cu12	(5.0; 5.0; -4.2)	(0.0; 0.0; 0.0)
6.018	Cu2-Cu9	(2.8; -5.0; -1.8)	(0.9; -1.7; -2.8)	8.228	Cu11-Cu14	(5.0; 5.0; -4.2)	(0.0; 0.0; 0.0)
6.018	Cu2-Cu13	(-5.0; 2.8; -1.8)	(1.7; -0.9; 2.8)				

- [1] R. Siddharthan and A. Georges, Square kagome quantum antiferromagnet and the eight-vertex model, *Phys. Rev. B* **65**, 014417 (2001).
- [2] I. Rousochatzakis, R. Moessner, and J. van den Brink, Frustrated magnetism and resonating valence bond physics in two-dimensional kagome-like magnets, *Phys. Rev. B* **88**, 195109 (2013).
- [3] S. S. Jahromi and Y. Iqbal, Quantum phase diagram of the spin- $\frac{1}{2}$ Heisenberg antiferromagnetic model on the square-kagome lattice, arXiv preprint (2025), arXiv:2503.07689 [cond-mat.str-el].
- [4] A. Ralko and I. Rousochatzakis, Resonating-Valence-Bond Physics Is Not Always Governed by the Shortest Tunneling Loops, *Phys. Rev. Lett.* **115**, 167202 (2015).
- [5] J. Merino and A. Ralko, Role of quantum fluctuations on spin liquids and ordered phases in the Heisenberg model on the honeycomb lattice, *Phys. Rev. B* **97**, 205112 (2018).
- [6] K. B. Yogendra, S. Karmakar, and T. Das, Symmetry, superposition, and fragmentation in classical spin liquids: A general framework and applications to square kagome magnets, *Phys. Rev. B* **110**, L060401 (2024).
- [7] O. Derzhko, J. Richter, O. Krupnitska, and T. Krokhnalskii, The square-kagome quantum Heisenberg antiferromagnet at

Bond distance (Å)	D	bond distance (Å)	D
3.114	13.9	6.234	0.2
3.278	27.7	6.381	0.0
4.404	8.9	6.555	0.0
5.009	11.0	7.084	2.7
5.266	1.9	7.717	0.0
5.340	0.0	7.761	0.0
5.614	0.0	7.805	0.1
5.727	0.8	7.807	0.0
5.769	0.7	8.120	0.0
6.018	3.3	8.228	0.0

TABLE V. Magnitudes $|D|$ (in K) of the Dzyaloshinskii–Moriya vectors for $\text{Na}_6\text{Cu}_7\text{BiO}_4(\text{PO}_4)_4\text{Cl}_3$ at $U = 6.66$ eV, grouped by Cu–Cu bond distance (in Å). This condensed summary complements Table IV by highlighting the distance dependence of the DM scale and the rapid suppression of the anisotropic exchange on longer bonds.

high magnetic fields: The localized-magnon paradigm and beyond, *Low. Temp. Phys.* **40**, 513 (2014).

- [8] Y. Hasegawa, H. Nakano, and T. Sakai, Metamagnetic jump in the spin- $\frac{1}{2}$ antiferromagnetic Heisenberg model on the square kagome lattice, *Phys. Rev. B* **98**, 014404 (2018).
- [9] K. Morita and T. Tohyama, Magnetic Phase Diagrams and Magnetization Plateaus of the Spin-1/2 Antiferromagnetic Heisenberg Model on a Square-Kagome Lattice with Three Nonequivalent Exchange Interactions, *J. Phys. Soc. Jpn.* **87**, 043704 (2018).
- [10] P. Tomczak and J. Richter, Specific heat of the spin-1/2 Heisenberg antiferromagnet on square kagome lattice, *J. Phys. A* **36**, 5399 (2003).
- [11] J. Richter, O. Derzhko, and J. Schnack, Thermodynamics of the spin-half square kagome lattice antiferromagnet, *Phys. Rev. B* **105**, 144427 (2022).
- [12] H. Nakano and T. Sakai, The Two-Dimensional $S=1/2$ Heisenberg Antiferromagnet on the Shuriken Lattice—A Lattice Composed of Vertex-Sharing Triangles—, *J. Phys. Soc. Jpn.* **82**, 083709 (2013).
- [13] J. Richter and J. Schnack, Magnetism of the $S = \frac{1}{2}J_1 - J_2$ square-kagome lattice antiferromagnet, *Phys. Rev. B* **107**, 245115 (2023).
- [14] M. Gembé, H.-J. Schmidt, C. Hickey, J. Richter, Y. Iqbal, and S. Trebst, Noncoplanar magnetic order in classical square-kagome antiferromagnets, *Phys. Rev. Res.* **5**, 043204 (2023).
- [15] P. Schmoll, A. Kshetrimayum, J. Naumann, J. Eisert, and Y. Iqbal, Tensor network study of the spin- $\frac{1}{2}$ Heisenberg antiferromagnet on the shuriken lattice, *Phys. Rev. B* **107**, 064406 (2023).
- [16] O. V. Yakubovich, L. V. Shvanskaya, G. V. Kiriukhina, A. S. Volkov, O. V. Dimitrova, and A. N. Vasiliev, Hydrothermal synthesis and a composite crystal structure of $\text{Na}_6\text{Cu}_7\text{BiO}_4(\text{PO}_4)_4[\text{Cl}(\text{OH})]_3$ as a candidate for quantum spin liquid, *Inorg. Chem.* **60**, 11450 (2021).
- [17] V. Popova, V. Popov, N. Rudashevskiy, S. Glavatskikh, V. Polyakov, and A. Bushmakin, Nabokoite $\text{Cu}_7\text{TeO}_4(\text{SO}_4)_5\text{KCl}$ and atlasovite $\text{Cu}_6\text{Fe}^{3+}\text{Bi}^{3+}\text{O}_4(\text{SO}_4)_5\text{KCl}$. New minerals of volcanic exhalations, *Zap. Vses. Mineral. Obsch.* **116**, 358 (1987).
- [18] F. Pertlik and J. Zemmann, The crystal structure of nabokoite, $\text{Cu}_7\text{TeO}_4(\text{SO}_4)_5 \cdot \text{KCl}$: The first example of a $\text{Te}(\text{IV})\text{O}_4$ pyramid with exactly tetragonal symmetry, *Mineral. Petrol.* **38**, 291 (1988).
- [19] B. Liu, Z. Zeng, A. Xu, Y. Sun, O. Yakubovich, L. Shvanskaya, S. Li, and A. Vasiliev, Low-temperature specific-heat studies on two square-kagome antiferromagnets, *Phys. Rev. B* **105**, 155153 (2022).
- [20] L. V. Shvanskaya, T. D. Bushneva, D. A. Chareev, L. S. Taran, V. V. Mazurenko, S. V. Streltsov, and A. N. Vasiliev, Buckle-Layered, Decorated Square-Kagome System $\text{KCu}_7\text{BiO}_4(\text{SO}_4)_5$, *Inorg. Chem.* **65**, 303 (2026).
- [21] A. F. Murtazoev, K. A. Lyssenko, M. M. Markina, V. A. Dolgikh, A. N. Vasiliev, and P. S. Berdonosov, New Nabokoite-like Phases $\text{ACu}_7\text{TeO}_4(\text{SO}_4)_5\text{Cl}$ ($A=\text{Na}, \text{K}, \text{Rb}, \text{Cs}$) with Decorated and Distorted Square Kagome Lattices, *Chem. Phys. Chem* **24**, e202300111 (2023).
- [22] M. Markina, P. Berdonosov, T. Vasilchikova, K. Zakharov, A. Murtazoev, V. Dolgikh, A. Moskin, V. Glazkov, A. Smirnov, and A. Vasiliev, Static and resonant properties of decorated square kagomé lattice $\text{KCu}_7(\text{TeO}_4)(\text{SO}_4)_5\text{Cl}$, *Mater. Chem. Phys.* **319**, 129348 (2024).
- [23] M. Fujihala, K. Morita, R. Mole, S. Mitsuda, T. Tohyama, S.-i. Yano, D. Yu, S. Sota, T. Kuwai, A. Koda, H. Okabe, H. Lee, S. Itoh, T. Hawaii, T. Masuda, H. Sagayama, A. Matsuo, K. Kindo, S. Ohira-Kawamura, and K. Nakajima, Gapless spin liquid in a square-kagome lattice antiferromagnet, *Nat. Commun.* **11**, 3429 (2020).
- [24] Y. Rebrov, V. Glazkov, A. Murtazoev, V. Dolgikh, and P. Berdonosov, High-frequency dielectric anomalies in a highly frustrated square kagomé lattice nabokoite family compounds $\text{ACu}_7(\text{TeO}_4)(\text{SO}_4)_5\text{Cl}$ ($A = \text{Na}, \text{K}, \text{Rb}, \text{Cs}$), *J. Magn. Magn. Mater.* **592**, 171786 (2024).
- [25] T. Goto, M. Fujihala, and S. Mitsuda, ^{27}Al -NMR study on a square-kagome lattice antiferromagnet, *Interactions* **245**, 40 (2024).
- [26] L. V. Shvanskaya, T. D. Bushneva, D. A. Chareev, L. S. Taran, V. V. Mazurenko, S. V. Streltsov, and A. N. Vasiliev, Buckle-layered, decorated square-kagome system $\text{kcu}_7 \text{ bio}_4 (\text{so}_4)_5$, *Inorganic Chemistry* **65**, 303 (2026).
- [27] M. G. Gonzalez, Y. Iqbal, J. Reuther, and H. O. Jeschke, Field-induced spin liquid in the decorated square-kagome antiferromagnet nabokoite $\text{KCu}_7\text{TeO}_4(\text{SO}_4)_5\text{Cl}$, *Commun. Mater.* **6**, 96 (2025).
- [28] I. Dzyaloshinsky, A thermodynamic theory of “weak” ferromagnetism of antiferromagnetics, *J. Phys. Chem. Solids* **4**, 241 (1958).
- [29] T. Moriya, Anisotropic Superexchange Interaction and Weak Ferromagnetism, *Phys. Rev.* **120**, 91 (1960).
- [30] L. Messio, O. Cépas, and C. Lhuillier, Schwinger-boson approach to the kagome antiferromagnet with Dzyaloshinskii-Moriya interactions: Phase diagram and dynamical structure factors, *Phys. Rev. B* **81**, 064428 (2010).
- [31] K. Mondal and C. Kadolkar, Schwinger boson mean-field theory of the kagome Heisenberg antiferromagnet with Dzyaloshinskii-Moriya interactions, *Phys. Rev. B* **95**, 134404 (2017).
- [32] N. Niggemann, N. Astrakhantsev, A. Ralko, F. Ferrari, A. Maity, T. Müller, J. Richter, R. Thomale, T. Neupert, J. Reuther, Y. Iqbal, and H. O. Jeschke, Quantum paramagnetism in the decorated square-kagome antiferromagnet $\text{Na}_6\text{Cu}_7\text{BiO}_4(\text{PO}_4)_4\text{Cl}_3$, *Phys. Rev. B* **108**, L241117 (2023).
- [33] D. P. Arovas and A. Auerbach, Functional integral theories of low-dimensional quantum Heisenberg models, *Phys. Rev. B* **38**, 316 (1988).
- [34] N. Read and S. Sachdev, Large- N expansion for frustrated quantum antiferromagnets, *Phys. Rev. Lett.* **66**, 1773 (1991).

- [35] L. O. Manuel, C. J. Gazza, A. E. Trumper, and H. A. Ceccatto, Heisenberg model with Dzyaloshinskii-Moriya interaction: A mean-field Schwinger-boson study, *Phys. Rev. B* **54**, 12946 (1996).
- [36] P. W. Anderson, New approach to the theory of superexchange interactions, *Phys. Rev.* **115**, 2 (1959).
- [37] T. Yildirim, A. B. Harris, A. Aharony, and O. Entin-Wohlman, Anisotropic spin Hamiltonians due to spin-orbit and Coulomb exchange interactions, *Phys. Rev. B* **52**, 10239 (1995).
- [38] D. I. Khomskii and S. V. Streltsov, Magnetic oxides, in *Encyclopedia of Condensed Matter Physics* (Elsevier, 2024) pp. 98–111.
- [39] D. I. Badrtdinov, O. S. Volkova, A. A. Tsirlin, I. V. Solovyev, A. N. Vasiliev, and V. V. Mazurenko, Hybridization and spin-orbit coupling effects in the quasi-one-dimensional spin- $\frac{1}{2}$ magnet $\text{Ba}_3\text{Cu}_3\text{Sc}_4\text{O}_{12}$, *Phys. Rev. B* **94**, 054435 (2016).
- [40] D. I. Badrtdinov, S. A. Nikolaev, A. N. Rudenko, M. I. Katsnelson, and V. V. Mazurenko, Nanoskyrmion engineering with *sp*-electron materials: Sn monolayer on a SiC(0001) surface, *Phys. Rev. B* **98**, 184425 (2018).
- [41] T. Lugan, L. D. C. Jaubert, and A. Ralko, Topological nematic spin liquid on the square kagome lattice, *Phys. Rev. Res.* **1**, 033147 (2019).
- [42] T. Lugan, L. D. C. Jaubert, M. Udagawa, and A. Ralko, Schwinger boson theory of the $J_1, J_2 = J_3$ kagome antiferromagnet, *Phys. Rev. B* **106**, L140404 (2022).
- [43] J. C. Halimeh and M. Punk, Spin structure factors of chiral quantum spin liquids on the kagome lattice, *Phys. Rev. B* **94**, 104413 (2016).
- [44] B. Schneider, J. C. Halimeh, and M. Punk, Projective symmetry group classification of chiral \mathbb{Z}_2 spin liquids on the pyrochlore lattice: Application to the spin- $\frac{1}{2}$ XXZ Heisenberg model, *Phys. Rev. B* **105**, 125122 (2022).
- [45] F. Wang and A. Vishwanath, Spin-liquid states on the triangular and Kagomé lattices: A projective-symmetry-group analysis of Schwinger boson states, *Phys. Rev. B* **74**, 174423 (2006).
- [46] O. Tchernyshyov, R. Moessner, and S. L. Sondhi, Flux expulsion and greedy bosons: Frustrated magnets at large N , *EPL* **73**, 278 (2005).
- [47] Additional subdominant Bragg peaks, carrying (i) 12% of the spectral weight of the dominant ones are located at $(2\pi - q, q)$, $(q, 2\pi - q)$, $(-(2\pi - q), 2q)$ and $(2q, -(2\pi - q))$ and (ii) carrying 4% intensity at $(-(2\pi - q), 2\pi - q)$, $(q, 2q)$ and $(2q, q)$.
- [48] J. Richter, J. Schulenburg, P. Tomczak, and D. Schmalfuß, The Heisenberg antiferromagnet on the square-kagomé lattice, *Condens. Matter Phys.* **12**, 507 (2009).
- [49] N. Astrakhantsev, F. Ferrari, N. Niggemann, T. Müller, A. Chauhan, A. Kshetrimayum, P. Ghosh, N. Regnault, R. Thomale, J. Reuther, T. Neupert, and Y. Iqbal, Pinwheel valence bond crystal ground state of the spin- $\frac{1}{2}$ Heisenberg antiferromagnet on the shuriken lattice, *Phys. Rev. B* **104**, L220408 (2021).